Desalination and Water Treatment
www.deswater.com
doi: 10.1080/19443994.2014.928801

54 (2015) 1361–1374
April

Taylor & Francis
Taylor & Francis Group

Evaluation of the effect of a hydraulic impeller in a flocculation basin on hydrodynamic behavior using computational fluid dynamics

Wen-Biao Fan[a,b], Wei-Guang Li[a,*], Xu-Jin Gong[a], Xin-Ran Zhang[a]

[a]*School of Municipal and Environmental Engineering, Harbin Institute of Technology, Harbin 150090, P.R. China, emails: fwb666@126.com (W.-B. Fan), kimkung@126.com (W.-G. Li), xujin_gong@126.com (X.-J. Gong), zhangxinranhit@163.com (X.-R. Zhang)*
[b]*Harbin Water Supply Group Co., Ltd, Harbin 150010, P.R. China*

Received 30 December 2013; Accepted 19 May 2014

ABSTRACT

This study investigates the hydraulic impeller in a flocculation basin, which is important to facilitate uniformity in the sedimentation basin and to improve sedimentation efficiency. The experiments were conducted in a Perspex vessel that is 100 × 100 × 700 mm (length × width × height), with an effective depth of 600 mm. A high resolution phase-resolved computational fluid dynamics (CFD) simulation technique was used. The mean velocity, root mean square velocity, and turbulent kinetic energy of different flow patterns were investigated. The commercial CFD software was used to process the data generated from the k–ε model. The velocity of the flow pattern can be predicted by k–ε model. The CFD software FLUENT was used to simulate the hydraulic impeller under various combinations. The turbulence kinetic energy k, the effective energy dissipation ε, velocity gradient G, and pressure were used as criteria to evaluate flocculation effects, to interpret the complex phenomenon in the course of flocculation, and to study the condition of the hydraulic impeller's influence on flocculation by varying the hydraulic impeller combinations. The influence of hydraulic conditions on flocculation can be interpreted by turbulence kinetic energy k, effective energy dissipation ε, velocity grad G, and pressure.

Keywords: Flocculation; Hydraulic impeller; Computational fluid dynamics (CFD); Fluent

1. Introduction

Flocculation plays an important role in drinking water treatment processes around the world. Proper design or optimization of the flocculation processes is essential to efficiently remove colloidal particles [1]. The complexity of the overall large scale flocculation process calls for its decomposition in two distinct conceptual components. The first part relates to the floc scale physico-chemical processes. This can be studied experimentally using laboratory equipment with a well-defined flow field, which can quantitatively assess the involved processes. The second conceptual component refers to large scale tank hydrodynamics and its interaction with the local physico-chemical

*Corresponding authors.

Presented at the 6th International Conference on the "Challenges in Environmental Science and Engineering" (CESE-2013), 29 October–2 November 2013, Daegu, Korea

1944-3994/1944-3986 © 2014 Balaban Desalination Publications. All rights reserved.

processes. Both components are crucial and must be taken into account to evaluate the flocculation process on a full scale.

Determining a solution for the governing equations in a macroscopic flow field is a very difficult task because of the geometrical complexity of most flocculation tanks and the existence of moving parts. Therefore, the model used in this study assumes that the contents are well mixed in the tank and the turbulence intensity is uniformly distributed [1]. However, it is also understood that the second assumption needs to be modified because turbulent intensity exhibits a very uneven distribution in the tank. An alternative approach to modify this assumption is the so-called compartmental modeling approach [2], which divides the tank into a finite number of well-mixed regions where each one has different but uniform properties. This approach permits a more detailed handling of the local physico-chemical processes. The most recent approach based on the combination of detailed floc-level treatment with detailed treatment of the macroscopic flow field using a computational fluid dynamics (CFD) code requires very high computational efforts. Simplifying the local scale problem by omitting physical parameters is not an appropriate approach to reduce the computational cost; instead, special mathematical techniques should be employed to reduce the degrees of freedom of the corresponding population balance equation.

The details of the geometry and the operation of the flocculation tank are, in most cases, more important than the details of the floc size distribution. Based on this account, the details on the size distribution can be reduced mathematically to save computational power. It must be noted that the literature on CFD simulations of waste water treatment is rather rich with cases where large mass fractions of solids lead to a two-way interaction between the liquid and solid phase [3,4]. However, this is not so for the much simpler problem of CFD simulation for potable water treatment where the solids mass fraction is low.

Particle removal efficiency decreases with decreasing particle size [5]. Therefore, flocs must be able to withstand shear energy applied to them in various different unit processes. When the degree of shear exceeds a threshold value, floc breakage will occur. However, the quantification of the energy requirements for floc breakage is not straightforward, and despite much work in this field, no standard strength test exists.

The literature contains examples of practical investigations into floc strength at the laboratory scale using a standard jar-test apparatus and procedure [6]. However, there is little reported research that has attempted to model the process using CFD. The research that has been published is limited in scope [7,8]. These papers have considered the flow fields generated by a small-scale flocculator and recognized the limitations of the existing design parameters. However, aside from qualitative analysis, none of the papers considered how these results would impinge on flocculation performance.

In this work, the effect of a new design of the hydraulic impeller flocculation reactor has been validated. The commercially available CFD code, Fluent 12, was used to model the flow field within the flocculator at the laboratory. The focus of this work concentrated on the development and application of simulation techniques and the analysis of computational models to increase the understanding of floc formation and breakage mechanisms. Previous work provided a quantitative analysis of floc growth and breakage [9]. The work reported here complements that previous work, providing a fundamental understanding of the hydrodynamic environments of which flocs are exposed to at a range of scales.

2. Materials and methods

2.1. CFD simulation

2.1.1. Tank parameters

The hydraulic impeller in the flocculator was rotated by water. The parameters of the structure and size are shown in Figs. 1 and 2. Hydraulic impeller operation parameters under different conditions (Cases 1–6) are illustrated in Table 1. The average flow rate (Q) was $3.6\,m^3/h$ and inlet velocity (V) was $0.1\,m/s$. The size of the tank was $100 \times 100 \times 700$ mm (length × width × height), with an effective depth of 600 mm.

2.2. Conceptual view of flocculation

Flocculation is the transformation of smaller destabilized particles into larger aggregates or flocs, with the rate of growth governed by the rate of interparticle collisions. Flocs are mass fractal objects that have an approximate density similar to water [8]. However, it was found that the density decreases with an increase in size; therefore, as the flocs grow in size, induced shear force may lead to floc breakage. The rate of floc growth is expressed conceptually using the following equation [10]:

$$R_{floc} = \alpha_{ij} R_{col} - R_{br} \quad (1)$$

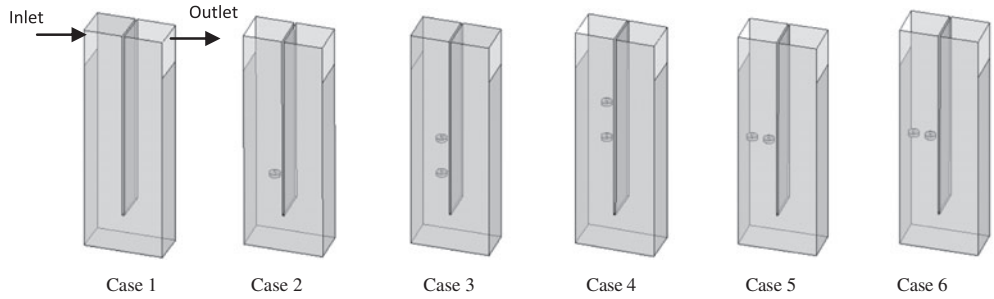

Fig. 1. Schematic of the hydraulic impeller in the flocculation basin used in the CFD simulation.

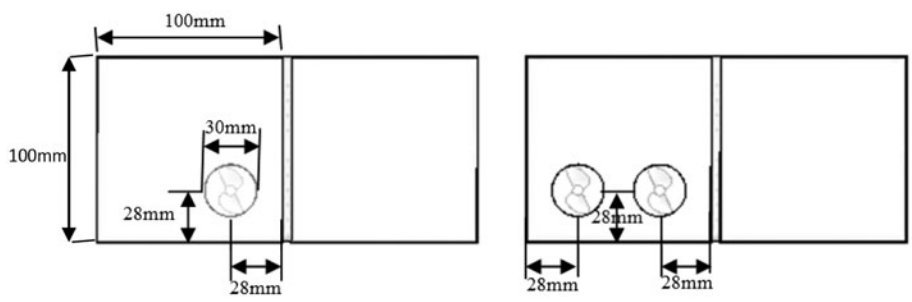

Fig. 2. Plan for the schematic of the hydraulic impeller in the flocculation basin.

Table 1
Blade operation parameters under different conditions

	Direction of rotation		Speed (rpm)		Height from the bottom (mm)	
	①	②	①	②	①	②
Case 1						
Case 2	Clockwise		120		200	
Case 3	Clockwise	Clockwise	120	165	200	300
Case 4	Clockwise	Clockwise	165	180	300	400
Case 5	Clockwise	Clockwise	85	165	300	300
Case 6	Clockwise	Counter clockwise	85	165	300	300

where R_{floc} represents the overall rate of floc growth and α is the collision efficiency factor ($0 < \alpha < 1$). R_{floc} and R_{br} are the rates of particle collision and floc breakage, respectively. The $\alpha_{ij}R_{col}$ is a function of ${}^{BM}\alpha_{ij}{}^{BM}R_{col_{ij}}$, ${}^{Sh}\alpha_{ij}{}^{Sh}R_{col_{ij}}$, and ${}^{DS}\alpha_{ij}{}^{DS}R_{col_{ij}}$, where i and j refer to discrete particles. *BM*, *Sh*, and *DS* refer to the collision mechanisms of Brownian motion, shear, and differential settlement, respectively.

Floc size can be considered to be a balance between the hydrodynamic forces exerted on a floc and the strength of the floc [10,11]. As a result, flocs do not continue to grow throughout the flocculation stage but rather attain a limiting size, of which breakage prevents further overall growth. For areas where the floc strength is resistant to the hydrodynamic forces, it is expected that either floc size will remain constant or growth will occur; for areas where the hydrodynamic forces exceed floc strength, floc breakage will occur. Consequently, the conceptual growth breakage mechanism may be expressed using the following equation [11]:

$$B = \frac{\text{Hydrodynamic forces}}{\text{Floc strength}} = \frac{F}{J} \tag{2}$$

where F represents the hydrodynamic forces exerted by the flow and J represents the strength of the floc. It is clear from Eq. (2) that breakage will occur when $B > 1$ and floc size will be maintained or increased when $B < 1$. Floc strength (J) is a function of the physico-chemical conditions (raw water type, coagulant type and dose) and the floc structure [12].

Previous studies have suggested that the hydrodynamic force required to pull apart a floc in a tensile mode may be expressed as Eq. (3) [11]:

$$F = \frac{\pi}{4}\sigma d^2 \tag{3}$$

where σ represents the hydrodynamic stress exerted on the floc and d is the area of the floc. In the viscous sub-range, $\sigma = \mu\sqrt{\varepsilon/v}$. Substituting into Eq. (2) shows that the breakage mechanism in the viscous sub-range, B_{VSR}, may be expressed as Eq. (4):

$$B_{VSR} = \frac{C_1\mu\sqrt{\varepsilon/vd^2}}{j} \tag{4}$$

where C_1 is a constant.

In the inertial sub-range:

$$\sigma = \bar{\rho}\cdot\bar{u}^2 \tag{5}$$

$$\text{where } \bar{u}^2 = C_2(\varepsilon\cdot d)^{2/3} \tag{6}$$

Substituting into Eq. (2) shows that the breakage mechanism in the inertial sub-range, B_{ISR}, may be expressed as Eq. (7):

$$B_{ISR} = \frac{C_2\rho\varepsilon^{2/3}\cdot d^{8/3}}{J} \tag{7}$$

where C_2 is a constant.

Consequently, it can be deduced from Eqs. (4) and (7) that floc size is dependent on the turbulence energy dissipation rate and floc strength, irrespective of sub-range. This is clearly of great significance towards the understanding of floc breakage mechanisms and limiting floc size as it directs workers to focus their efforts towards ε and J. Thus, it is both the physico-chemical and turbulent conditions within the containing vessel that controls the flocculation process. In water treatment, the velocity gradient term is used to characterize mixing and thereby predict aggregation kinetics and break-up phenomena.

2.3. The equations of the model

2.3.1. Flow-field equations

The flow-field equations governing the 3D flow in a tank are:

Continuity equation:

$$\frac{\partial\rho}{\partial t} + div(\rho u) = 0 \tag{8}$$

Momentum equations:

$$\frac{\partial u_i}{\partial u_t} + \frac{\partial u_i u_j}{\partial x_j} = \frac{\partial P}{\partial x_i} + \frac{\partial}{\partial x_j}\left(\frac{\partial u_i}{\partial x_j} - \rho\bar{u}_i\bar{u}_j\right) + g_i\rho \tag{9}$$

where t is the time, x_i is the Cartesian coordinate in the i direction, u_i is the flow velocity in the i direction, ρ is the density of water, P is the pressure, μ is the molecular viscosity of the water, and g_i is the acceleration of gravity.

For the calculation of the Reynolds (turbulent) stresses $-\rho u_i u_{j,}$ the assumption of the applied isotropic turbulence is combined with the Boussinesq approximation.

$$-\rho\bar{u}_i\bar{u}_j = \mu_t\left(\frac{\partial u_i}{\partial x_j} + \frac{\partial u_j}{\partial x_i}\right) - \frac{2}{3}\left(\rho k + u_t\frac{\partial u_i}{\partial x_j}\right)\delta_{ij} \tag{10}$$

where μ_t is the eddy viscosity, δ_{ij} is the Kronecker delta ($\delta_{ij} = 1$ for $i = j$ and $\delta_{ij} = 0$ for $i = j$), and k is the average turbulent kinetic energy per unit mass, which is given by:

$$k = \frac{1}{2}\left(\bar{u'^2} + \bar{v'^2} + \bar{w'^2}\right) \tag{11}$$

The inlet Reynolds numbers for the investigated tanks ranged from 90,000 to 400,000. The standard k–ε turbulence model assumes that the flow is fully turbulent, molecular viscosity can be ignored, and the calculation and analysis of the flow field is for low turbulence intensity, of which the decrease in the complexity of the calculations is consistent with the actual flow field. These assumptions are in accordance with the hydraulic characteristics of flocculation reactor designed in this study. Therefore, the standard k–ε turbulence model was chosen for the determination of the distribution of μ_t via k and the rate of its dissipation ε [13].

$$\mu_t = \rho c_\mu\frac{k^2}{\varepsilon} \tag{12}$$

where c_μ is an empirical constant and ε is given by the following equation:

$$\varepsilon = \frac{\mu}{\rho}\overline{\left(\frac{\partial u_i'}{\partial x_k}\right)\left(\frac{\partial u_i'}{\partial x_k}\right)} \tag{13}$$

The distributions of k and ε are calculated from the following semi-empirical-modeled transport equations:

$$\frac{\partial(\rho k)}{\partial t} + \frac{\partial(\rho k u_i)}{\partial x_i} = \frac{\partial}{\partial x_i}\left[\left(\mu + \frac{\mu_i}{\sigma_k}\right)\frac{\partial k}{\partial x_i}\right] + G_k + G_b - \rho\varepsilon - Y_M + S_K \tag{14}$$

$$\frac{\partial(\rho \varepsilon)}{\partial t} + \frac{\partial(\rho \varepsilon u_i)}{\partial x_i} = \frac{\partial}{\partial x_i}\left[\left(\mu + \frac{\mu_i}{\sigma_\varepsilon}\right)\frac{\partial \varepsilon}{\partial x_i}\right] + C_{1\varepsilon}\frac{\varepsilon}{k}(G_k + C_{3\varepsilon}G_b) - C_{2\varepsilon}\rho\frac{\varepsilon^2}{k}S_\varepsilon \tag{15}$$

For incompressible flow, without considering the source terms of custom $G_b = 0$, $Y_M = 0$, $S_\varepsilon = 0$, $S_k = 0$, the model constants $C_{2\varepsilon} = 1.92$, $C_\mu = 0.09$, $\sigma_\varepsilon = 1.3$, $\sigma_k = 1.0$. In this model, for each component of the *Reynolds* stress, it was assumed that the viscosity coefficient μ is the same, where μ_t is an isotropic scalar. In the case of bend flow, where turbulent flow is anisotropic, μ_t is anisotropic tensor. G is the production term of k by the mean velocity gradients defined as follows:

$$G = \mu_t\left(\frac{\partial u_i}{\partial x_j} + \frac{\partial u_j}{\partial x_i}\right)\frac{\partial u_i}{\partial x_j} \tag{16}$$

The standard values of the constants $C_{1\varepsilon} = 1.44$, $C_{2\varepsilon} = 1.92$, $C_\mu = 0.09$ and of the turbulent Schmidt numbers $\sigma_\varepsilon = 1.3$, and $\sigma_k = 1.0$ are used in the present computations.

2.4. Numerical details

2.4.1. The numerical code

Calculations were performed with the numerical code Fluent 12 [14]. This code has been applied in various liquid or gas engineering problems [15,16]. The code uses the finite control volume method for the spatial discretization of the domain. The equations of the model are integrated over each control volume, such that the relevant quantity is conserved in a discrete sense for each control volume. For the continuity equation (pressure–velocity coupling), a second-order central difference approximation is used. It is modified by a fourth-order derivative in pressure, which redistributes the influence of pressure. The second-order upwind Euler scheme approximates the transient term. A scalable and fully implicit coupled solver is used for the solution of the equations.

2.4.2. Boundary conditions

Boundary conditions are defined at the borders of the computation domains, where inlet is velocity and outlet is outflow. The free surface was treated as a symmetry plane use the rigid lid approximation.

2.4.3. Numerical grids

The numerical code employs unstructured numerical grids, which permit an accurate representation of the boundaries. The computational grids for the nine cases ranged from 110,000 to 200,000 tetrahedral elements with grid refinement in the inlet and outlet regions. These sizes were selected after a series of preliminary calculations to ensure grid independent results.

2.5. Experimental model and method

2.5.1. Experimental model

Two modeling reactors were introduced in the present work—the hydraulic impeller baffle flocculation reactor (HIB-FR) and traditional grid flocculation reactor (G-FR). The configuration of HIB-FR, which is an innovative modification of the G-FR, is shown in Fig. 3. The new HIB-FR was established by

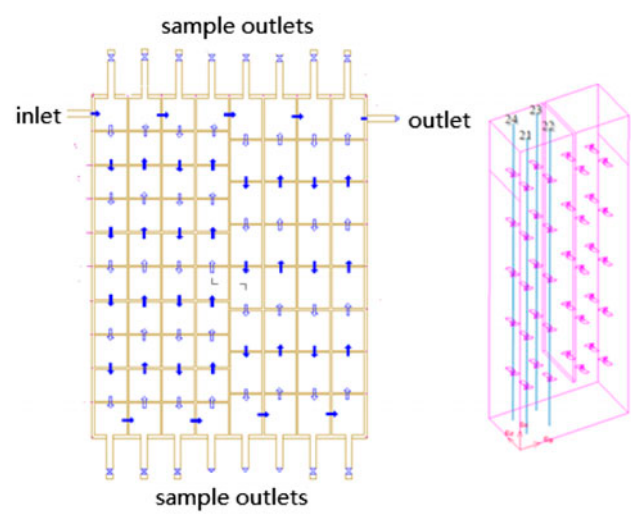

Fig. 3. Experimental setup of HIB-FR.

introducing hydraulic impeller spoiler in the G-FR, which aims to change the fluid flow state and to create a favorable vortex in the flocculation process. HIB-FR contains eight corridors. In the first four corridors, each corridor is made up of ten grids ($L \times B \times H = 100 \times 100 \times 700$ mm). Each corridor has eight grids ($L \times B \times H = 100 \times 120 \times 700$ mm) for another four corridors. The design flow for each reactor, either HIB-FR or G-FR, is 2–4 m^3/h and the hydraulic retention time is 7.2–14.4 min. The effectiveness of the HIB-FR was investigated using four operation modes. In each operation condition, spoiler components of HIB-FR were designed according to the following:

Case-A: Hydraulic impellers with the same rotation directions were settled in the first four corridors (such as Case 5 in Fig. 1).

Case-B: Symmetrically rotational hydraulic impellers were settled in the first four corridors (such as Case 6 in Fig. 1).

Case-C: Hydraulic impellers with the same rotation directions were settled in the first two corridors (as Case 5). Symmetrically rotational hydraulic impellers were settled in the third corridor (as Case 6). None of hydraulic impellers were settled in other corridors.

Case-D: In this case, none of hydraulic impeller was settled in the corridors, and HIB-FR was operated as a traditional G-FR. G-FR has the same configuration and size as HIB-FR.

2.5.2. Experimental method

The raw water used in the present work was surface-water from the Songhua-River during two different periods in Harbin. The turbidity of the raw water samples in the two periods was 148.3 and 18.02 NTU, respectively. During the experiment, the turbidity of raw water was measured every 2 h. Parameters of other water qualities are illustrated in Table 2. Because the Harbin plant is a widely used water plant, polymeric aluminum chloride (PAC) was used as flocculants for the present work. Table 2 also shows parameters of PAC dosage under different quantities of raw water. The flow rate and reaction time were 3.6 m^3/h and 8 min, respectively. Raw water was pumped to a pipeline mixer to complete the mixing process with PAC, and then the mixture entered the flocculation reactor. After 8 min of operation, effluent water was sampled in a beaker (1,000 mL) for static sedimentation. Turbidity was measured at a different time from static sedimentation.

3. Results and discussion

3.1. CFD simulation results

3.1.1. Velocity

As shown in Fig. 4, a strong swirl occurred in Cases 2–6 in comparison with Case 1. The formation of the swirl can result in a great increase in the axial and radial velocity of the particles. Changes in velocity can consequently promote the chance of collisions between adjacent particles. The adjacent coaxial hydraulic impellers (Cases 2 and 3) form a strong vortex, which consequently provides sufficient energy for the formation of micro-vortices. The radially adjacent hydraulic impeller (Cases 5 and 6) formed many little vortices and micro-vortices. In particular, the hydraulic impeller (Case 5) that rotated in the same direction formed a large number of micro-vortices, which provided favorable hydraulic conditions for the formation of flocs.

3.1.2. Turbulence kinetic energy

As shown in Fig. 5, higher turbulent kinetic energy occurred around the blade area. The turbulent kinetic energy in Cases 2–6 decreases gradually as a function of the increase in distance to the blade area. The scope of a single blade is approximately 50 mm; the average value of turbulence kinetic energy k is approximately $8 \times 10^{-4}\ m^2/s^2$. The results suggested that coaxial hydraulic impeller in Cases 3 and 4 produced larger turbulent kinetic energy with two energy peaks around the adjacent blades area. This phenomenon can be used to improve the mixing and hydrolysis reaction of the flocculant. In Cases 5 and 6, the radial adjacent hydraulic impeller could increase the opportunity of particle collisions at an earlier stage of the flocculation reaction and consequently increase floc formation. The adjacent hydraulic impeller with the

Table 2
Parameters of raw water quality and PAC dosage

Sample code	Water temperature (℃)	pH	Turbidity (NTU)	PAC dosage (mg/L)
1	24	6.81	148.3	21
2	1	6.80	18.02	30

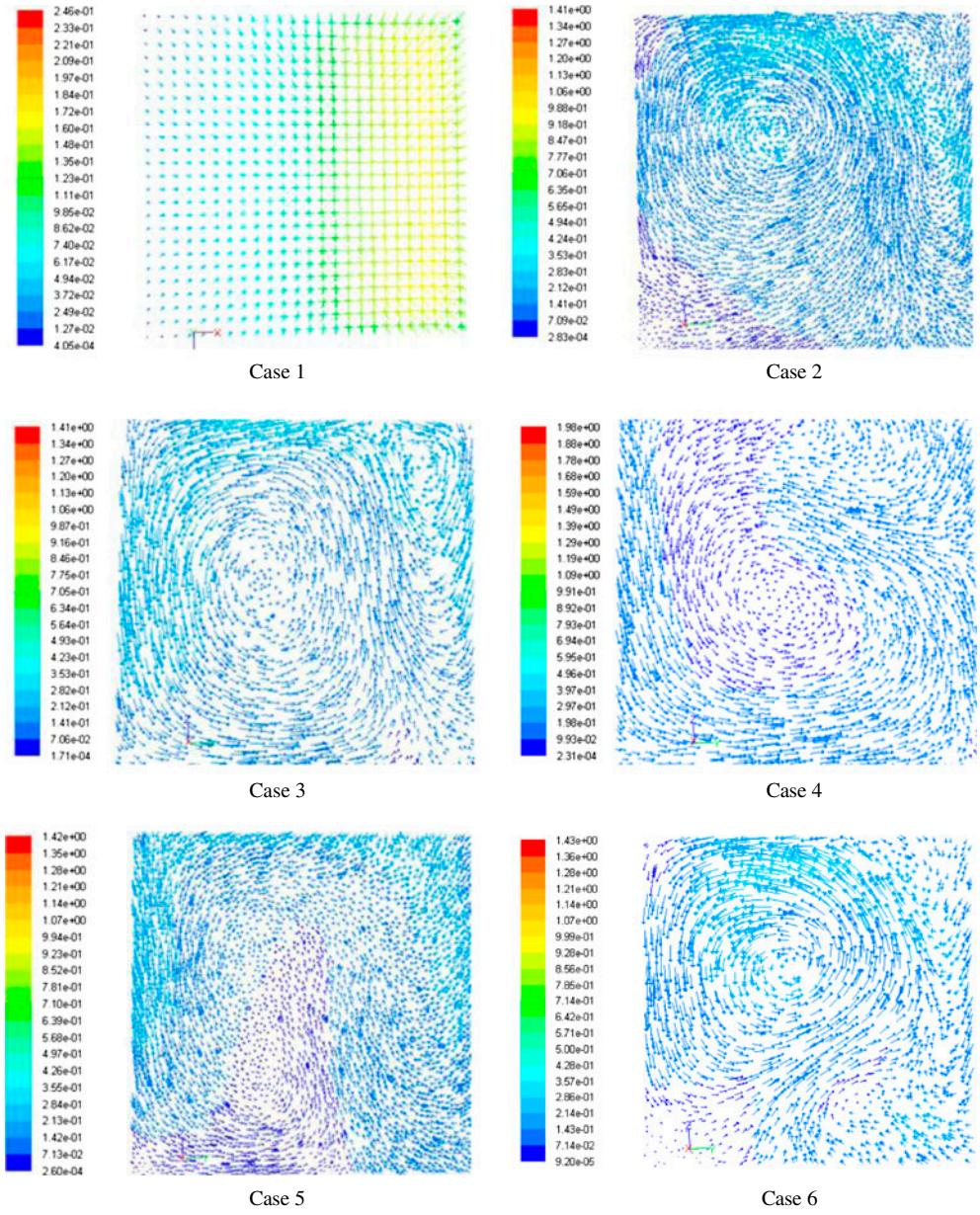

Fig. 4. Vertical map of the distribution of the velocity vectors.

same rotation direction in Case 5 may result in the increase of particle collisions. The rotational symmetry of the impeller in Case 6 can help to reduce the shear force for flocs and avoid floc breakage.

3.1.3. Turbulence dissipation rate

The results in Fig. 6 and Table 3 suggest that the average of turbulence dissipation rate (ε) in Case 1, which did not have the hydraulic impeller, was approximately $1.11 \times 10^{-3} m^2/S^3$. The introduction of the hydraulic impeller in Cases 2–6 lead to the promotion of the turbulence dissipation rate (ε) around the area of the hydraulic impeller. The average value of turbulence dissipation rate (ε) increased to approximately $5.28 \times 10^{-3} m^2/S^3$ in Cases 2–6. In addition, the higher turbulence dissipation rate (ε) occurred around the areas of the adjacent coaxial hydraulic impeller in Case 3 ($5.84 \times 10^{-3} m^2/S^3$) and Case 4 ($9.35 \times 10^{-3} m^2/S^3$). With the radial adjacent hydraulic impeller, turbulence dissipation rate (ε) in Cases 5 and 6 became more uniform. From the perspective of energy conversion, the increase

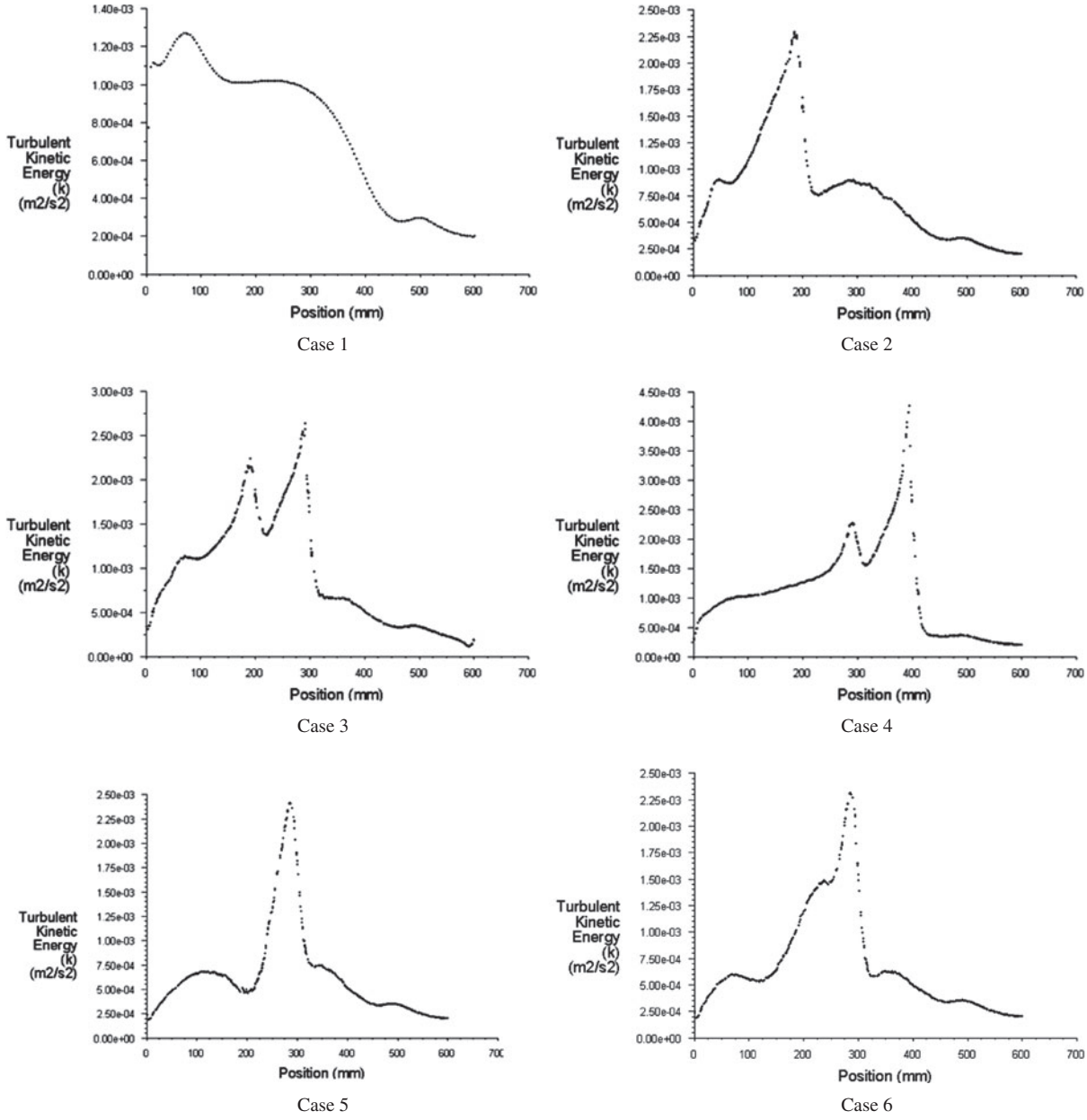

Fig. 5. Variation in local turbulence kinetic energy in basin.

of the turbulence dissipation rate around the area of the hydraulic impeller (Cases 2–6) is conducive to the formation of flocs.

3.1.4. Velocity gradient

Fig. 7 shows that the average velocity gradient has been greatly improved due to the introduction of hydraulic impeller, as in Cases 2–6. The particle size distribution of flocs can also become more reasonable in comparison with Case 1. Obviously, velocity gradient in Case 1 is uneven, showing a trend of fluctuation, whereas the adjacent hydraulic impeller in Cases 5 and 6 created more uniform and reasonable distribution of velocity gradient. This phenomenon is more conducive for the netting role of floc to form larger size floc in the late stages of the flocculation reaction.

3.1.5. Pressure

Fig. 8 shows that the introduction of the hydraulic impeller caused an obvious fluctuation in the water pressure, relating to the position and distribution of impellers in Cases 2–6.

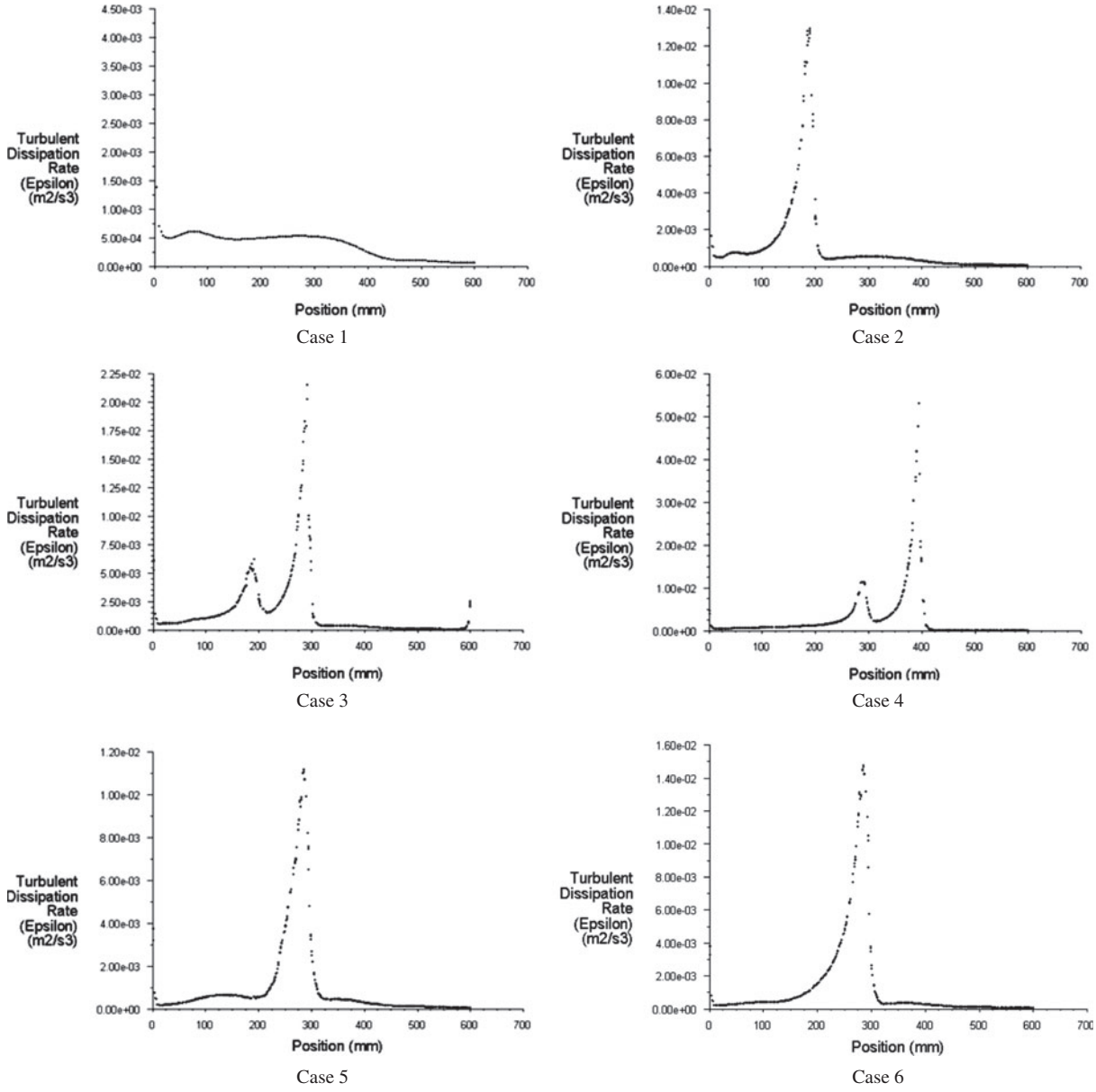

Fig. 6. Variation in the local turbulence dissipation rate in the basin.

In comparison with other cases, the variation of the pressure transition was much more reasonable in Cases 3 and 4. This indicates that the density of flocs will become more compact in Cases 3 and 4, and floc breakage can also be avoided. Consequently, higher efficiency can also be achieved in the sedimentation process.

3.2. Experimental verification

3.2.1. Effects of flocculation reaction time on coagulation and sedimentation

The flow rate of the HIB-FR was 3.6 m^3/h. At the residence times of 4, 5, 6, 7, and 8 min, water samples were taken from the reactor for static sedimentation (30 min) in a 1,000-mL beaker. The results under two levels of turbidity of raw water, 148.3 and 18.02 NTU, are illustrated in Figs. 9 and 10, respectively.

As shown in Fig. 9, the flocculation-sedimentation efficiency of the hydraulic impeller flocculation reactor (Case-A/B/C) was greater than the G-FR at a different retention time. Higher sedimentation efficiencies were obtained due to the introduction of the hydraulic impeller in Case-A/B/C. The best residual turbidity (2.21 NTU) occurred after 7 min of flocculation in Case-C. The results also suggested that the effluent turbidity under Case-A/B/C reached stability after

Table 3
Volume integral values of turbulent kinetic energy, turbulence dissipation rate, and velocity gradient

	Turbulent kinetic energy (K)			Turbulence dissipation rate (ε)			Velocity gradient G (1/s)		
	Max (10^{-4} m^2/s^2)	Min (10^{-4} m^2/s^2)	Volume average (10^{-4} m^2/s^2)	Max (m^2/s^3)	Min (10^{-5} m^2/s^3)	Avg (10^{-5} m^2/s^3)	Max (1/s)	Min (1/s)	Avg (1/s)
Case 1	37.2543	0.0825	10.8814	1,384	0.4632	111.6566	30.1461	0.0369	3.1631
Case 2	2,433.702	0.16	7.6617	7,548.11	3.4854	346.4504	144,532.7	0.0399	6.8606
Case 3	2,743.049	0.0644	8.8231	9,347.095	0.9063	583.5831	144,364.8	0.0743	7.9318
Case 4	4,460.00	0.2047	10.8784	13,727.87	0.1636	934.859	211,083.9	0.0407	8.1460
Case 5	2,663.5050	0.071	7.2602	8,820.044	1.0536	389.3409	144,131.5	0.0400	7.2774
Case 6	2,425.6317	0.082	8.1649	7,984.1172	1.3061	390.6936	138,998.5	0.0402	7.2031

5 min static sedimentation, while Case-D required 7 min to reach turbidity stability without the hydraulic impeller. Stable flocs formed at the flocculation time of 5 min in Case-B, and the effluent turbidity entered a platform (approximately 3.2 NTU) after 5 min. However, the flocculation morphology changed in Case-A and Case-C after 6 min of flocculation, it could be attributed to the occurrence of a secondary flocculation.

Case-C was the combination of Case 5 (the same rotation directions of the hydraulic impeller in the first two corridors) and Case 6 (symmetrically rotational hydraulic impellers in the third corridor). From the analysis of Cases 5 and 6 in Figs. 4–7, k, ε, and G increased in the first and second corridors of Case 5, which can increase the probability of particle collisions and improve the efficiency of flocculation. Moreover, the rotational symmetry hydraulic impeller in Case 6 can help to reduce the turbulent shear stress on the flocs. Generally, more reasonable values of k, ε, and G occurred in HIB-FR (Case-A/B/C) (Section 3.1). Therefore, the distinct differences between Case-A/B/C and Case-D can be attributed to the changes of turbulence kinetic energy k, turbulence dissipation rate ε, and velocity gradient G in the flocculation process. Moreover, Case-C achieved less shear stress in the process of floc formation, which can reduce the breakage of flocs.

The efficiencies of HIB-FR for low temperature and low turbidity water were also investigated under Cases-A, B, C, and D. As shown in Fig. 10, the results suggest that Case-B achieved greater flocculation-sedimentation efficiency than Case-A, C, and D. It required 6 min for Case B to achieve better flocculation-sedimentation efficiency (5.69 NTU), which was lower than the grid reactor (8.82 NTU in Case-D). Moreover, it was difficult to form an effective flocculation nucleus in low temperature and low turbidity water because of loose floc, which was easily broken and had a lower efficiency for secondary flocculation. Case-B was the application of Case 6 in HIB-FR (symmetrically rotational hydraulic impellers in the third corridor). As mentioned in Section 3.1, the case can form more reasonable hydraulic conditions in comparison to Case 6. Therefore, Case-B has a higher efficiency for the flocculation process in low temperature and low turbidity water.

3.2.2. Effects of flocculation reaction time on coagulation and sedimentation

The effect of sedimentation time was also investigated in relation to the two levels of turbidity of raw water, 148.3 and 18.02 NTU. The results are illustrated in Figs. 11 and 12. As shown in Fig. 11, Case-C, a combination of Cases 5 and 6, achieved the optimal sedimentation efficiency, reaching 2.74 NTU after 30 min. However, G-FR (Case-D) required a longer sedimentation time (40 min) to reach a stable turbidity (3.46 NTU). The hydraulic conditions in Case-A was beneficial to form floc at the earlier stage of flocculation, however, stronger shear forces can cause floc breakage. Despite the reduction of broken flocs in Case-B, its hydraulic conditions for the formation of flocs was not more favorable than the hydraulic conditions of Case-A in the initial stages of flocculation. Case-C combines the advantages of Case-A and Case-B. Therefore, Case-C can greatly improve the hydraulic conditions for floc formation, reduce the probability of broken flocs, avoid the occurrence of secondary flocculation, and achieve greater flocculation-sedimentation efficiency for high turbidity raw water (Fig. 11).

The effects of sedimentation time for low temperature and low turbidity water were also investigated under Case-A, B, C, and D. As shown in Fig. 12, the results suggested that greater sedimentation efficiencies occurred in Cases-B and C. After 40 min of sedimentation in Cases-C and B, the turbidity decreased

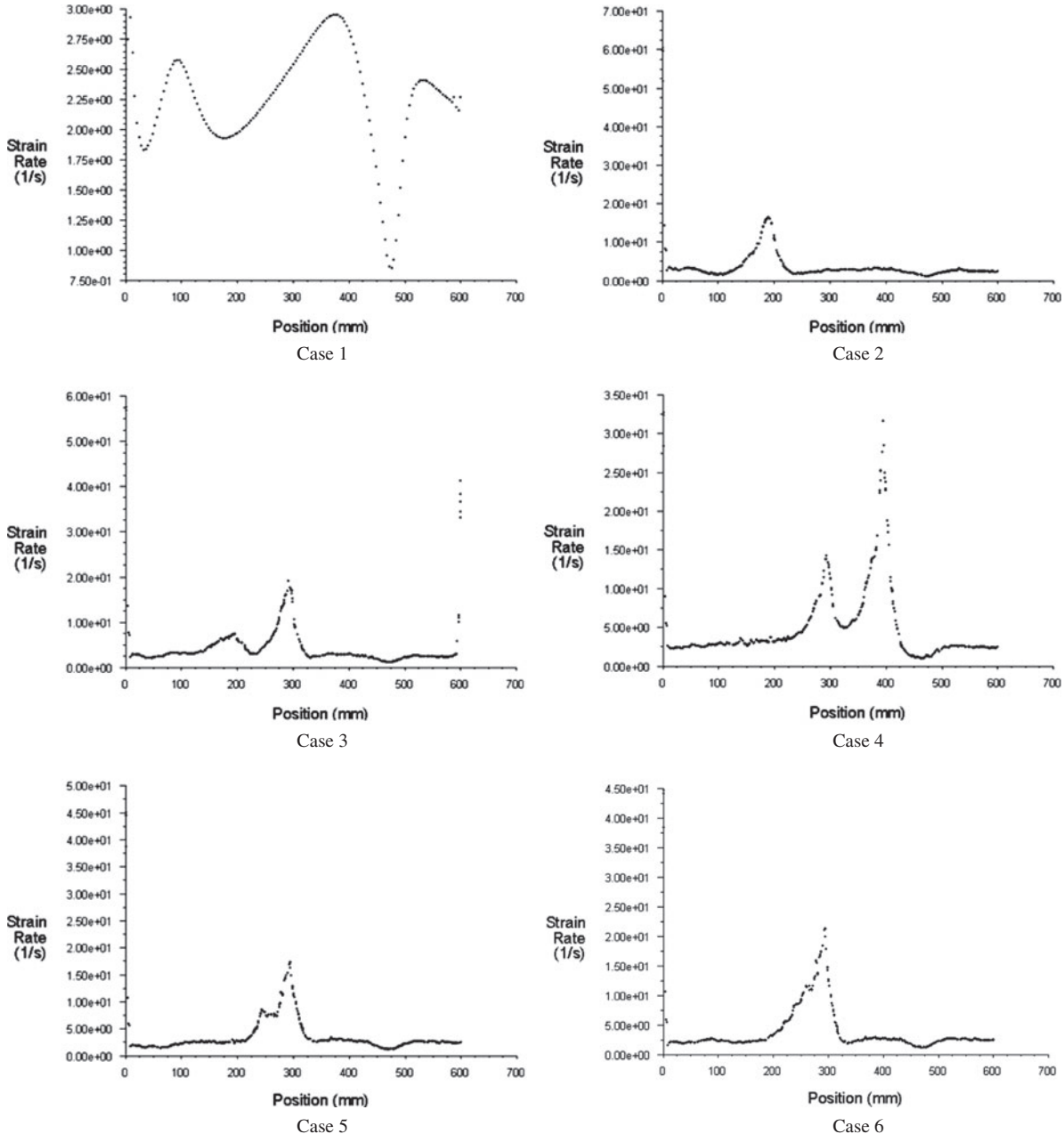

Fig. 7. Variation in the local velocity gradient in basin.

to approximately 2.46 and 1.87 NTU, respectively. However, after 60 min of sedimentation, the turbidity for Case-D (G-FR) and Case-A gradually stabilized at 6.35 and 4.49 NTU, respectively. Therefore, Case-B can lead to the greatest sedimentation efficiency for low temperature and low turbidity water. Moreover, flocs formed in low temperature and low turbidity water were loose, low in density and easily broken, and had less secondary flocculation. Therefore, it is significantly important to maintain accurate and reasonable hydraulic conditions during the flocculation process. As mentioned in Section 3.2.1, k, ε, and G values in Case-B ensured uniform and reasonable hydraulic conditions. Therefore, Case-B was selected for flocculation process for the low temperature and low turbidity water.

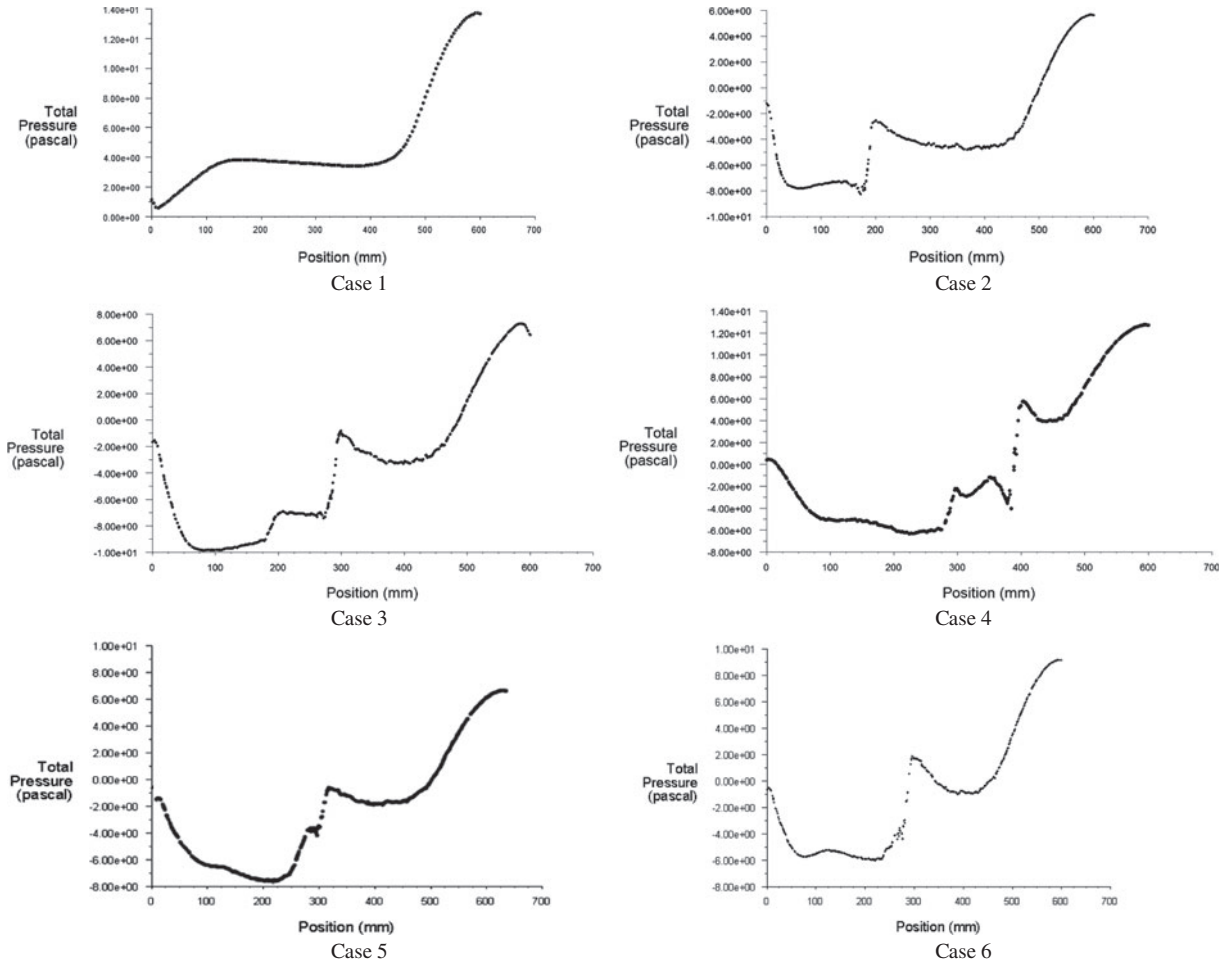

Fig. 8. Variation in the local pressure in the basin.

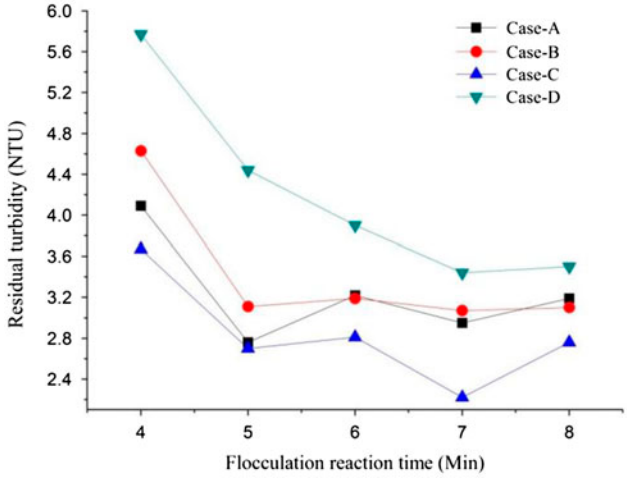

Fig. 9. The residual turbidity after different flocculation reactions when raw water turbidity is 148.3 NTU.

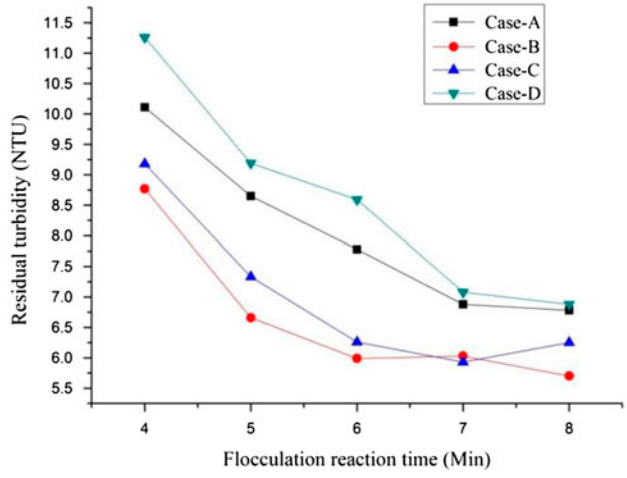

Fig. 10. The residual turbidity after different flocculation reaction times when raw water turbidity is 18.02 NTU.

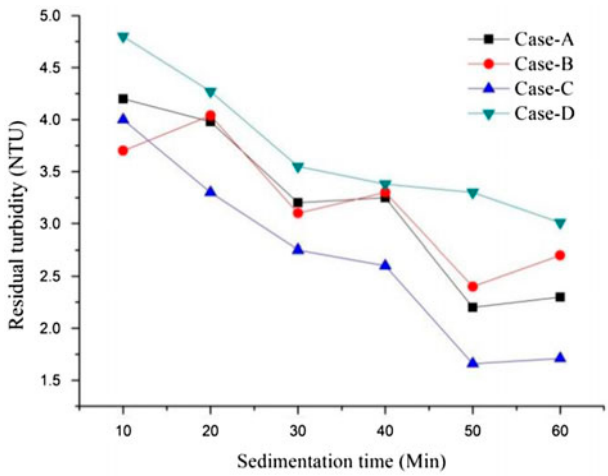

Fig. 11. The residual turbidity after different sedimentation times when raw water turbidity is 148.3 NTU, water temperature is 28℃, and pH is 6.81.

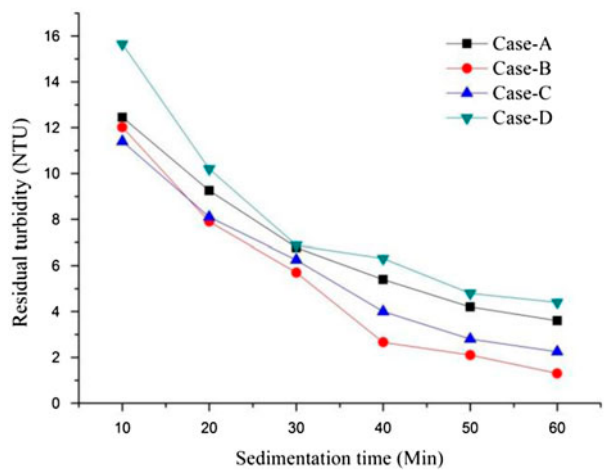

Fig. 12. The residual turbidity after different sedimentation time when raw water turbidity is 18.02 NTU (raw water turbidity = 8.02 NTU; water temperature = 2.9℃; pH 6.80).

4. Conclusions

This paper has demonstrated the range of scales and applications to which CFD can be applied successfully to flocculation processes used for drinking water treatment. The very efficient computational tool developed here can be used for the design and optimization of the geometric and operational characteristics of the water treatment process. For the hydraulic impeller flocculator, the coaxial adjacent blade can effectively increase local turbulent intensity. The radial adjacent blade contributes to an evenly distributed velocity gradient G, the turbulent kinetic energy k, and turbulence dissipation rate ε. Blades in the same direction of rotation can be used to improve particle collision probability and enhance the density of the floc. Blades in symmetrical rotation reduce the shear force of flocs, increase particle collision probability at the same time, and reduce the breakage of flocs. In the flocculation reaction stage, using the hydraulic impeller to adapt to different combinations of flocculation kinetics law can effectively improve the flocculation effect and reduce the dosage of flocculant. Using modest computing hardware, CFD modeling is restricted to the analysis of relatively simple flows. More complex scenarios, such as rotating meshes, require greater computing power, which is not generally found outside academic environments or specialized consultancies. CFD modeling also requires trained staff to generate robust models and solutions. The effective integration of these two factors is contributed to the widespread use of CFD in most water companies and mainstream consultancies in the foreseeable future.

Acknowledgments

This study was supported by the "Special project of application technology research and development plan of Heilongjiang province" (Funding No. GA13C302).

References

[1] N. Birjandi, H. Younesi, N. Bahramifar, S. Ghafari, A.A. Zinatizadeh, S. Sethupathi, Optimization of coagulation-flocculation treatment on paper-recycling wastewater: Application of response surface methodology, J. Environ. Sci. Health A, Toxic/Hazard. Sub. Environ. Eng. 48 (2013) 1573–1582.
[2] J. Ponou, T. Ide, A. Suzuki, H. Tsuji, L.P. Wang, G. Dodbiba, T. Fujita, Evaluation of the flocculation and de-flocculation performance and mechanism of polymer flocculants, Water Sci. Technol. 69 (2014) 1249–1258.
[3] A. Besson, P. Guiraud, High-pH-induced flocculation-flotation of the hypersaline microalga Dunaliella salina, Bioresour. Technol. 147 (2013) 464–470.
[4] K. Ramalingam, S. Xanthos, M. Gong, J. Fillos, K. Beckmann, A. Deur, J.A. McCorquodale, Critical modeling parameters identified for 3D CFD modeling of rectangular final settling tanks for New York City wastewater treatment plants, Water Sci. Technol. 65 (2012) 1087–1094.
[5] H. Casanova, E. Dickinson, Rheology and flocculation of oil-in-water emulsions made with mixtures of αs1-Casein + β-Casein, J. Colloid Interface Sci. 207 (1998) 82–89.
[6] R. Divakaran, V.N. Pillai, Flocculation of kaolinite suspensions in water by chitosan, Water Res. 35 (2001) 3904–3908.

[7] P.W. Longest, M.J. Oldham, Mutual enhancements of CFD modeling and experimental data: A case study of 1-mum particle deposition in a branching airway model, Inhalation Toxicol. 18 (2006) 761–771.
[8] S. Xanthos, K. Ramalingam, S. Lipke, B. McKenna, J. Fillos, Implementation of CFD modeling in the performance assessment and optimization of secondary clarifiers: The PVSC case study, Water Sci. Technol. 68 (2013) 1901–1913.
[9] M. Franceschi, A. Girou, A.M. Carro-Diaz, M.T. Maurette, E. Puech-Costes, Optimisation of the coagulation-flocculation process of raw water by optimal design method, Water Res. 36 (2002) 3561–3572.
[10] P. Jarvis, B. Jefferson, J. Gregory, S.A. Parsons, A review of floc strength and breakage, Water Res. 39 (2005) 3121–3137.
[11] D. Bouyer, C. Coufort, A. Line, Z. Do-Quang, Experimental analysis of floc size distributions in a 1-L jar under different hydrodynamics and physicochemical conditions, J. Colloid Interface Sci. 292 (2005) 413–428.
[12] C.T. Tanneru, J.D. Rimer, S. Chellam, Sweep flocculation and adsorption of viruses on aluminum flocs during electrochemical treatment prior to surface water microfiltration, Environ. Sci. Technol. 47 (2013) 4612–4618.
[13] A.M. Djerdjev, R.J. Hunter, J.K. Beattie, Self-depletion flocculation of tetralin oil-in-water emulsions, Langmuir 22 (2006) 84–87.
[14] M.H. Sohn, S.A. Douglass, M.C. Chen, J.R. Anderson, Characteristics of fluent skills in a complex, dynamic problem-solving task, Human Factors 47 (2005) 742–752.
[15] R. Chanamai, N. Herrmann, D.J. McClements, Ultrasonic spectroscopy study of flocculation and shear-induced floc disruption in oil-in-water emulsions, J. Colloid Interface Sci. 204 (1998) 268–276.
[16] X. Shao, L. Lynd, C. Wyman, Kinetic modeling of cellulosic biomass to ethanol via simultaneous saccharification and fermentation: Part II. Experimental validation using waste paper sludge and anticipation of CFD analysis, Biotechnol. Bioeng. 102 (2009) 66–72.